Physics in Medicine & Biology

IPEM Institute of Physics and Engineering in Medicine

ACCEPTED MANUSCRIPT

Monte Carlo calculation of the relative TG-43 dosimetry parameters for the INTRABEAM electronic brachytherapy source

To cite this article before publication: David Santiago Ayala Alvarez *et al* 2020 *Phys. Med. Biol.* in press https://doi.org/10.1088/1361-6560/abc6f1

Monte Carlo calculation of the relative TG-43 dosimetry parameters for the INTRABEAM electronic brachytherapy source

David Santiago Ayala Alvarez, Peter G F Watson, Marija Popovic, Veng Jean Heng, Michael D C Evans, and Jan Seuntjens

Medical Physics Unit, McGill University and Cedars Cancer Center, Montreal, Canada

E-mail: david.ayalaalvarez@mail.mcgill.ca

Abstract. The INTRABEAM system (Carl Zeiss Meditec AG, Jena, Germany) is an electronic brachytherapy device designed for intraoperative radiotherapy applications. To date, the INTRABEAM x-ray source has not been characterized according to the AAPM TG-43 specifications for brachytherapy sources. This restricts its modeling in commercial treatment planning systems (TPSs), with the consequence that the doses to organs at risk are unknown. The aim of this work is to characterize the INTRABEAM source according to the TG-43 brachytherapy dosimetry protocol. The dose distribution in water around the source was determined with Monte Carlo (MC) calculations. For the validation of the MC model, depth dose calculations along the source longitudinal axis were compared with measurements using a soft x-ray ionization chamber (PTW 34013) and two synthetic diamond detectors (microDiamond PTW TN60019). In our results, the measurements in water agreed with the MC model calculations within uncertainties. The use of the microDiamond detector yielded better agreement with MC calculations, within estimated uncertainties, compared to the ionization chamber at points of steeper dose gradients. The radial dose function showed a steep fall-off close to the INTRABEAM source (<10 mm) with a gradient higher than that of commonly used brachytherapy radionuclides (^{192}Ir, ^{125}I and ^{103}Pd), with values of 2.510, 1.645 and 1.232 at 4, 6 and 8 mm, respectively. The radial dose function partially flattens at larger distances with a fall-off comparable to that of the Xoft Axxent® (iCAD, Inc. Nashua, NH) electronic brachytherapy system. The simulated 2D polar anisotropy close to the bare probe walls showed deviations from unity of up to 55% at 10 mm and 155°. This work presents the MC calculated TG-43 parameters for the INTRABEAM, which constitute the necessary data for the characterization of the source as required by a TPS used in clinical dose calculations.

Keywords: electronic brachytherapy, brachytherapy dosimetry, TG-43, Monte Carlo, INTRABEAM

1. Introduction

The INTRABEAM system (Carl Zeiss Meditec AG, Jena, Germany) was initially developed in the 1990s for interstitial radiosurgical treatments of intracranial cancer metastases (Douglas et al. 1996). With the inclusion of new applicators for the source, the system use was expanded to treat other sites such as rectal cancer and peripheral soft tissue sarcomas, and since 1998 it is mainly employed for the treatment of breast cancer patients with intraoperative radiotherapy (IORT) (Gunderson et al. 2011). The INTRABEAM system contains a miniature linear accelerator that drives electrons towards a gold target where 50 kVp x rays are produced. In addition to the different applicators available with the INTRABEAM, the system includes a control console where the treatment parameters are set and monitored, and this is connected to a user terminal for treatment plan verification (Eaton 2012).

Absorbed dose in water from the INTRABEAM can be determined at a point of interest using in-water depth dose data along the source axis provided by the manufacturer. The dose curves can be verified by measuring with a PTW 34013 ionization chamber in a water phantom available from Zeiss (Sethi et al. 2018, Carl Zeiss Meditec AG 2011). Independent dosimetry protocols traceable to primary standards for electronic brachytherapy (eBT) sources have recently been investigated and constitute an open field of research. In the past three years, Watson *et al* (2017, 2018, 2019) developed a protocol to independently determine the absorbed dose to water from the INTRABEAM source using a Monte Carlo (MC) calculated factor, C_Q, which accounts for beam quality changes at different depths in water for the INTRABEAM spectra. However, they found that the C_Q correction factor is highly dependent on the geometry of the ionization chamber. The geometry dependence plays an important role in the PTW 34013 ionization chamber used in the experiments, as its response is highly dependent on the plate separation which is not accurately known from chamber to chamber. Large tolerances in the reported geometry specifications for plate separation and the detector's effective point of measurement (EPOM) of the PTW 34013 ionization chamber lead to high uncertainties in the absorbed dose estimation of up to 23% (Watson et al. 2017). Further research with alternative radiation dosimeters is therefore motivated.

Treatment planning with the INTRABEAM system is generally limited to determining the treatment time based on the tabulated values of depth dose rate for a calibrated source and the prescription dose at a depth of interest. This method fails to provide 3D dose distribution, letting unknown the doses to organs at risk. The limitations of this approach are particularly evident in the treatment of glioblastoma (INTRAGO protocol) (Giordano et al. 2014), where external beam radiotherapy (EBRT) planning must be performed with consideration of delivered doses during the intraoperative treatment. Organ constraints of the dose distribution of the combined intraoperative and external beam treatments require accurate knowledge of the INTRABEAM dose distribution. In 2015, Valdivieso-Casique et al. (2015)

developed a treatment planning system (TPS) for INTRABEAM, called RADIANCE (GMV Innovating Solutions, Madrid, Spain), using a hybrid MC-based algorithm (Vidal et al. 2014). RADIANCE was originally developed in 2007 for dose calculations with electron IORT and it has yet to become widely deployed for use in INTRABEAM treatment planning. The present work is geared towards the data acquisition and validation of dosimetric parameters that characterize the INTRABEAM source in a way that could be implemented in widely available commercial treatment planning software for brachytherapy sources. The brachytherapy TPSs based on the AAPM TG-43 protocol allow a fast acquisition of 3D dose distributions in water and are available in almost all radiotherapy facilities (Nath et al. 1995, Rivard et al. 2004). This approach is parallel to that of Rivard et al. (2006) who studied the brachytherapy parameters from the Xoft Axxent® (iCAD, Inc. Nashua, NH) electronic x-ray source based on the AAPM TG-43 protocol. For the INTRABEAM source, the TG-43 parameters have not been determined, to our knowledge.

This work addresses issues with the INTRABEAM dosimetry and presents determined TG-43 dosimetry parameters for the INTRABEAM source, using MC simulations. These functions could, in certain situations, be used in commercial TPSs for efficient dose calculations in IORT. The MC model has been validated by measuring in water with the PTW 34013 ionization chamber and with the PTW TN60019 microDiamond detector.

2. Materials and Methods

2.1. INTRABEAM source geometry

With the INTRABEAM system, electrons produced in the electron gun are accelerated with a Gaussian distribution of energy with mean of 50 keV and full width at half maximum (FWHM) of 5 keV (Clausen et al. 2012). The electrons are then transported in vacuum towards the tip of the 10 cm long, 3.2 mm outer diameter probe and collide with a 0.5 μm thick gold target that covers the inner surface of the hemispherical end of the source (Dinsmore et al. 1996, Yanch & Harte 1996). As a result, x rays of approximately 50 kVp are produced by bremsstrahlung and fluorescence. The metallic probe wall is surrounded by thin biocompatible layers and its 16 mm distal part is substituted by a beryllium x-ray window (Yanch & Harte 1996, Nwankwo et al. 2013). The INTRABEAM source was modeled using the egs++ library (Kawrakow et al. 2009) of EGSnrc, based on a compilation of data available from publications and manufacturer specifications. The starting point of the geometry and MC model of the source for this work was previously developed and provided by Watson *et al* (2017, 2018), with few variations. The materials and geometry data were mainly obtained from specifications provided by Nwankwo et al. (2013) as presented in table 1. A geometry reconstruction diagram used in our simulations is shown in figure 1.

Accurate simulations of the source probe must include a detailed model of the

Table 1. Materials specifications of the INTRABEAM source according to Nwankwo *et al* (2012) (table edited from Watson et al. (2017)).

Materials		Thickness (μm)	Density (g cm^{-3})
Target	Au	1.0	19.32
Body	Be	500	1.85
Biocompatible layers	NiO	2.5	6.67
	Ni	2.5	8.90
	CrN	2.5	5.90

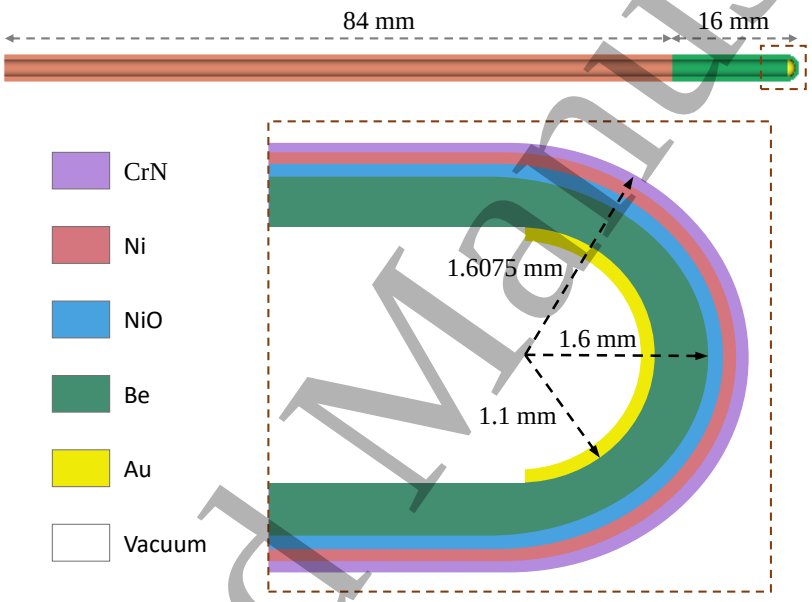

Figure 1. Reconstruction of the INTRABEAM source geometry used for the MC simulations. The inset below (not to scale) shows the magnified cross-sectional view of the source tip with the beryllium window, the gold target and the biocompatible layers materials and dimensions, as used in this work (materials specification adapted from Nwankwo et al. (2013)).

effective distribution of particles impinging onto the gold target. The electron beam is internally deflected in the evacuated needle using a magnetic beam deflector that causes the electron beam to oscillate about the probe's central axis (Clausen et al. 2012, Biggs & Thomson 1996, Moradi et al. 2017). According to the manufacturer, the deflection is induced to improve the polar symmetry of the dose distribution around the source. Different approaches to model the internal electron beam deflections can be found in the literature. For this regard, the present work followed the results of the investigation by Clausen et al. (2012), who modeled the beam in a way that the incoming electrons hit the gold target in the shape of two concentric rings of radii 0.6 to 0.7 mm and 0.7 to 0.8 mm, with weighting factors of 1.05 and 1.55, respectively. We used egs++

to construct the particle source proposed by Clausen *et al* as a combination of two collimated sources generating hollow cones with apex at the proximal end of the probe, and projecting the required rings 10 cm downstream on the base of the gold target. This particle source model generated with a continuous ring sweeping approximation will be called '*ring-shaped source*' throughout this document, and is the reference for our MC calculations. We have investigated the effect of the particle source geometry on the dose distributions in water by comparing the 2D anisotropy parameter obtained from the *ring-shaped source* with a homogeneous parallel circular source, or '*circular-shaped source*', which does not account for the internal beam deflection. Furthermore, recent studies have shown that the beam oscillation is also pulsed, generating a segmented distribution of x-ray emission spots on the gold target. The geometry of the focal spots has been measured by Sievers *et al* (Sievers et al. 2011, Schneider 2017) using a pinhole camera. In order to assess the effect of the spots in the beam generation, we simulated an alternative particle source, the '*spotted-shaped source*', using the model previously proposed by Abudra'A (2017), consisting of sixteen homogeneous and parallel electron source spots equally spaced at the base of the gold target. A Gaussian energy distribution with a mean energy of 50 keV and FWHM of 5 keV was used in our *ring-shaped source* and *spotted-shaped source* calculations. For the *circular-shaped source*, a monoenergetic electron beam of 50 keV was used. The internal beam deflection of the *ring-shaped source* and *spotted-shaped source* models, together with the Gaussian distribution in energy, were not assessed before in the original *circular-shaped source* model provided by Watson *et al* (2017, 2018, 2019).

2.2. Radiation transport parameters

The dose distribution in water around the source was determined with MC calculations using the egs_brachy (v2017.09.15) (Chamberland et al. 2016) user code of the EGSnrc code system. For the low-energy range of photons usually observed in brachytherapy, egs_brachy allows rapid dose calculations by approximating dose to electronic kerma obtained via a tracklength estimator, utilizing new dedicated variance reduction techniques for eBT sources. In this study, simulations were run from the interactions of the electron beam striking the gold target using the transport parameters predefined in an EGSnrc input file. All the EGSnrc physics processes for low-energy photons were included in our simulations, as for example Rayleigh scattering, bound Compton scattering, photoelectric absorption and atomic relaxations for K, L, M and N shells. PENELOPE libraries were used for electron impact ionization. The photon and bremsstrahlung cross sections were modeled using the XCOM (Berger et al. 2010) and NRC (Kawrakow & Rogers 2019) databases, respectively. The transport cut-off energy for photons (PCUT) was set at 1 keV, and for electrons (ECUT) inside the source was set at 512 keV (1 keV kinetic energy). Electrons were not transported outside the source (ECUT = 1 MeV) because dose was approximated as electronic kerma, and was calculated using the mass energy-absorption coefficients for water

(ρ = 1.0 g cm^{-3}) provided by egs_brachy in a data file. Cross-section data for the materials in the source model were generated covering the energy range from 1 keV to 1.5 MeV, ensuring accurate transport modelling of the simulated low-energy photons and electrons. Variance reduction techniques used include bremsstrahlung cross-section enhancement in the gold target by a factor of 50, uniform bremsstrahlung splitting with a factor of 100, and the associated statistical weights corrections using Russian roulette.

The MC model of the source was validated by comparing the measurements in water with the simulations using two different dosimeters. The egs_chamber user code (Wulff et al. 2008) of EGSnrc was employed for the validation due to the available variance reduction techniques for dose profile calculations with radiation detectors. The same transport parameters described in the previous paragraph for egs_brachy calculations were employed and additional variance reduction techniques were included, namely, the intermediate phase-space storage was used to obtain data from particles entering a pre-defined volume enclosing all the chamber positions, and then used to generate the profiles. In addition, photon cross-section enhancement in the proximity of the cavity regions was used and the statistical weights were corrected using range-based Russian roulette. A summary of the MC simulation details is presented in table 2, following the recommendations of the AAPM TG-268 report (Sechopoulos et al. 2018).

2.3. TG-43 parameters

The specific dimensions of the INTRABEAM source are proprietary, but the effective x-ray focal spot is small (less than 1 mm). Following the approach of Rivard et al. (2006) for the Xoft system, we have used the 2D formalism of the TG-43 with a point-source approximation to describe the geometry function, $G_{\rm p}(r,\theta) = 1/r^2$, and radial dose function, $g_{\rm p}(r)$, but accounting for the 2D polar anisotropy, $F(r,\theta)$, close to the source probe. In this way, the dose rate at any point $P(r,\theta)$ in water can be determined from the dose rate at a reference point $P(r_0,\theta_0)$ as

$$\dot{D}(r,\theta) = S_{\rm K}\,\Lambda \left(\frac{r_0}{r}\right)^2 g_{\rm p}(r)\,F(r,\theta), \qquad (1)$$

where the product of air-kerma strength of the source, $S_{\rm K}$, and the dose-rate constant, Λ, provides the dose rate at $P(r_0,\theta_0)$, and the accompanying functions determine the corrections for geometry, scattering and attenuation in water in the 2D distribution. According to the specifications of the INTRABEAM source geometry, azimuthal symmetry around the source long axis is assumed (Dinsmore et al. 1996, Yanch & Harte 1996).

The parameters $g_{\rm p}(r)$ and $F(r,\theta)$ of (1) were calculated with MC. For this, the coordinate system origin was located at the source tip, and $\theta = 0^\circ$ points towards the distal part of the source as illustrated in figure 2. Dose rates were scored in a set of annular bins centered at the source longitudinal axis covering the region z = [-50, 50] mm and d = [0, 50] mm in 0.4 mm intervals in both the longitudinal and radial directions. Although TPSs require data in more extended volumes, points located outside the

Table 2. Summary of the characteristics of the MC method used to obtain the TG-43 parameters.

Item	Description	References
Code	EGSnrc 2019	Kawrakow & Rogers (2019)
	egs++ library, EGSnrc 2019 master branch	Kawrakow et al. (2009)
	egs_brachy (v2017.09.15)	Chamberland et al. (2016)
	egs_chamber, EGSnrc 2019 master branch	Wulff et al. (2008)
Validation	Validated with two sets of measurements: **1.** Using a water phantom provided by the source manufacturer and a soft x-ray ionization chamber (PTW 34013) **2.** With a customized setup using a Wellhöfer water tank and two synthetic diamond detectors (microDiamond PTW TN60019)	
Timing	Time required to obtain the dose distribution in water: ∼7 h with a cluster of 124 cores split in five nodes of Intel(R) Xeon(R) CPU models: two E5-2697 v3 @ 2.60 GHz, two E5-2687W @ 3.10 GHz and one Gold 6140 @ 2.30 GHz. The time required for the PDDs with the ion chamber and the diamond was ∼120 h and ∼27 h, respectively	
Source description	Divergent electron beam hitting the target in the shape of two concentric rings. Gaussian energy distribution centered at 50 keV with FWHM of 5 keV	Clausen et al. (2012)
Cross-sections	Photoelectric and Rayleigh scattering: XCOM	Berger et al. (2010)
	Compton: relativistic impulse approximation	Kawrakow & Rogers (2019)
	Bremsstrahlung: NRC	Kawrakow & Rogers (2019)
	Electron impact ionization: PENELOPE	Bote & Salvat (2008)
	Atomic relaxations with explicit M and N-shell transitions: EADL	Watson & Seuntjens (2016)
Transport parameters	Boundary crossing algorithm: Exact	Kawrakow & Rogers (2019)
	PCUT = 1 keV. ECUT inside the source = 512 keV. Electrons were not transported outside the source (ECUT = 1 MeV)	
Variance reduction techniques	Bremsstrahlung and photon cross-section enhancement, uniform bremsstrahlung splitting, intermediate phase-space storage, range-based Russian roulette	Chamberland et al. (2016), Wulff et al. (2008)
Scored quantities	For dose distribution: absorbed dose to water (collision kerma approximation)	
	For PDDs: absorbed dose to air and diamond	
# histories /statistical uncertainty	Water: 3×10^9/0.07%–0.3% at 10–40 mm on the source axis. Ion chamber: 1.5×10^{10}/2.4%–3.6% at 10–40 mm. Diamond: 1.5×10^9/0.7%–1% at 10–40 mm	
Statistical methods	History-by-history	Chamberland et al. (2016)
Postprocessing	Data normalized at 10 mm from the source axis along the transverse plane at the source tip	

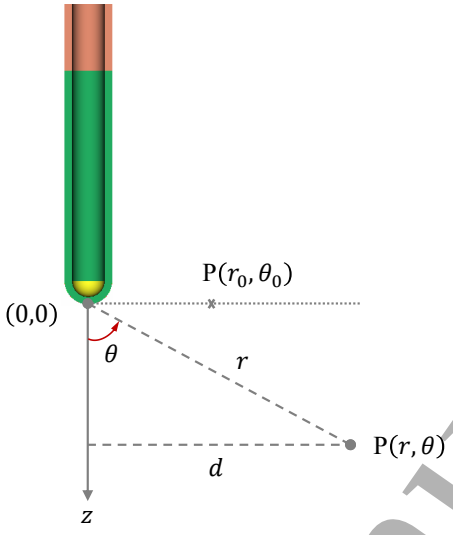

Figure 2. Reference coordinate system used for determining the TG-43 parameters for the INTRABEAM source.

chosen region lead to dose rates too low to measure reproducibly. These also require considerably longer computing time to reduce uncertainties to acceptable values. This volume was chosen as a representative volume since most of the dose delivery occurs near the source and the MC model can be accurately validated in this region. The scoring volume composition consisted of liquid water of mass density 1.0 g cm^{-3} and atomic composition 2:1 for H:O, and was immersed in a bigger spherical phantom of radius 20 cm and the same water composition to ensure full scattering conditions in the scoring volume (Rivard et al. 2006, Hiatt et al. 2015). The water phantom and scoring volume were centered at the source tip. In order to obtain sufficient statistics, 3×10^9 histories were run resulting in type A uncertainties (k = 1) in the range 0.07% to 0.3% at 10 to 40 mm from the source tip over the source longitudinal axis, and from 0.01% to 0.02% at 10 to 50 mm on the transverse plane.

2.4. Validation of the MC model

The MC *ring-shaped source* model was validated by comparing depth dose calculations against measurements in water and results of previous investigations (Watson et al. 2017). Data used in the validation correspond to the measurements and calculations of the dose to the detector's radiation sensitive volume (RSV), along the source longitudinal axis, and at distances measured from the source tip.

2.4.1. Measurements with ionization chamber. A set of measurements was carried out in water using a water phantom provided by the source manufacturer, a PTW air-kerma calibrated parallel-plate ionization chamber, model 34013, connected to a PTW UNIDOS E electrometer, and an INTRABEAM source (S/N: 507366). The PTW 34013

(a) (b)

Figure 3. (a) Experimental setup for measurements with the PTW 34013 ionization chamber in a Zeiss water phantom. The ionization chamber is placed in the plastic holder below the source needle. (b) Experimental setup for measurements with the PTW TN60019 microDiamond detector in a Wellhöfer water phantom. The detector is placed in a plastic holder attached to the Wellhöfer automated 3D scanning system (WP700, version V 3.51.00, Wellhöfer, Germany). The drawn red circle encloses an in-house built accessory constructed to bypass the INTRABEAM interlock system when no applicator is attached.

ion chamber model is not waterproof, therefore, it is placed inside a water proofing holder built into the side wall of the water tank. The setup for the measurements with the ion chamber is shown in figure 3(a). The holder was included in the MC simulations using the geometry and material specifications provided by the manufacturer.

The measurements in the present work follow the methodology and recommendations described by Watson et al. (2017), based on the Zeiss water phantom manual (Carl Zeiss Meditec AG 2015). Charge data were acquired from 60 s readings for each ionization chamber position, which was precisely moved along the central axis of the source. When the probe tip is in contact with the external surface of the water proofing holder, the position of the detector's EPOM is determined as: $r_1 = x_{\mathrm{H}} + x_{\mathrm{A}} + x_{\mathrm{IC}}$, where x_{H} is the holder wall thickness (printed on the holder, corresponds to 1.018 mm in our case), x_{A} is the air gap between the inside of the holder wall and the upper surface of the ion chamber housing (x_{A} is a constant of 0.5 mm), and x_{IC} is the distance from the upper surface of the ion chamber housing to the chamber's EPOM (x_{IC} is reported as 0.26 mm in the calibration certificate of the ion chamber used). Once the EPOM's initial position is determined ($r_1 = 1.778$ mm in our case), it is possible to change the probe to EPOM distance by moving the probe upwards using the Z direction adjustment knob of the water tank. The detector's EPOM was shifted from 2 to 50 mm depth from the source

tip in increasingly larger steps ranging from 0.4 to 2 mm. Measurements were repeated three times in each chamber position and the mean values and standard deviations were determined. The results of the present investigation were also compared with the measurements performed by Watson et al. (2017) with a different INTRABEAM source (S/N: 507535) to assess possible systematic errors.

2.4.2. Measurements with microDiamond detectors. Synthetic diamond detectors represent a promising alternative to the PTW 34013 ionization chamber as they exhibit advantageous dosimetric properties. Specifically, they present a well defined and validated geometry, and a small RSV able to correct for volume averaging effects in high dose gradients observed close to the INTRABEAM source. These detectors were thus deemed suitable for measurement and employed in our experiments. The Zeiss water phantom was designed to be used exclusively with the PTW 34013 ionization chamber; therefore, a different phantom with a more flexible setup was required for the measurements with a synthetic PTW TN60019 microDiamond detector. The Wellhöfer water tank with a 3D scanning system (WP700, version V 3.51.00, Wellhöfer Dosimetrie (IBA), Germany) was used to position the microDiamond detector with 0.5 mm precision. This setup is shown in figure 3(b). The microDiamond detector was connected through a triaxial cable to a Keithley electrometer, model 6517A (Keithley Instruments, Inc., Cleveland, U.S.A.). Measurements with the microDiamond detector were performed along the source longitudinal axis at 2 to 50 mm depth in water from the source tip in increasingly larger steps ranging from 1 to 5 mm. For user and patient safety in clinical IORT treatments, the INTRABEAM system cannot be operated with the source held by the INTRABEAM arm without the use of an applicator. In order to perform measurements with the bare probe, an in-house built accessory was constructed to bypass the INTRABEAM interlock system, as can be seen attached to the distal part of the arm in figure 3(b). To assess reproducibility of the measurements, two microDiamond detectors were used and the data sets were averaged.

As for the ionization chamber, a model of the microDiamond detector was available and used in the MC simulations. The relative dose to RSV of the detector calculations were directly compared to the relative measurements of detector signal, and no conversion to dose to water was required. This implies that non-intrinsic beam quality dependence was accounted for in the calculations. Our study did not take into account the intrinsic beam quality dependence of the response, which was shown to increase substantially with reducing effective photon energy from 375 keV to below 13 keV (Kaveckyte et al. 2020). Below 50 keV, however, the response variation shows more variability depending on the assumed sensitive volume thickness. More data on the response of microDiamond detectors in low-energy kV beams is needed to derive an accurate correction factor for this effect.

2.5. Uncertainty analyses

The evaluation of uncertainties on the absorbed dose from the INTRABEAM system was performed following the guidance of the AAPM TG-43U1 report (Rivard et al. 2004) updated for photon-emitting brachytherapy sources in the TG-138 report (DeWerd et al. 2011). Under this approach, type A (statistical) and type B (systematic) uncertainties are determined by following the International Organization for Standardization Guide to the Expression of Uncertainty in Measurement (ISO GUM) recommendations (BIPM, IEC, IFCC, ISO, IUPAC, IUPAP and OIML 1995). The following analyses are performed for the measurements and calculations of the dose rates along the source longitudinal axis at 10 mm ($\dot{D}$(10 mm, 0°)) and at 40 mm ($\dot{D}$(40 mm, 0°)). Expanded uncertainties with a coverage factor of two (k = 2), which defines a confidence level of 95% in normal distributions (DeWerd et al. 2011), is recommended for the analyses of the results presented in the current report.

2.5.1. Measurement uncertainties. Type A uncertainties on the measured detector signal correspond to the standard deviation of the mean of a series of three consecutive readings at each detector position. For the ionization chamber, the standard deviations of the mean for charge measurements were 0.02% and 0.09% at 10 and 40 mm, respectively. For the two microDiamond detectors, average standard deviations of the mean of 0.2% and 0.3% were obtained at the same depths. All the remaining uncertainties are considered to be type B. The positioning precision in the Zeiss water phantom to achieve the desired source to detector distance was ±0.1 mm. The influence of this parameter on the dosimetric uncertainty was determined as the difference in dose rate at each depth in water when applying an offset of ±0.1 mm to the fitted depth dose curve. The uncertainties in detector reading due to positioning uncertainty at 10 and 40 mm were 2.2% and 0.7%, respectively, for the Zeiss phantom with the ionization chamber. The same procedure is followed with the Wellhöfer phantom, which has a precision of ±0.5 mm. In this case, reading uncertainties due to positioning, averaged for both microDiamond detectors, were 14% and 4.8% at 10 and 40 mm, respectively. No correction for measurement medium were required since measurements and MC calculations were performed directly in water. The combined standard uncertainties (k = 1) are completely dominated by the positioning uncertainty, with total values of 2.2% and 0.7% for measurements with the PTW 34013 ionization chamber at 10 and 40 mm, respectively, and 14% and 4.8% as the average for measurements with both diamond detectors.

2.5.2. Calculation uncertainties. In the MC simulations, type A uncertainties are attributed to those statistical fluctuations reported by scoring volume in the '.3ddose' file from the egs_brachy application, and in the '.egslog' files from egs_chamber. Reported uncertainties (k = 1) at 10 and 40 mm for the calculation of dose to water with egs_brachy are 0.07% and 0.3%, respectively. Uncertainties in the absorbed dose to

the RSV of the ionization chamber with egs_chamber were 2.4% and 3.6%, and for the synthetic diamond were 0.7% and 1.0% at 10 and 40 mm, respectively. The impact of the plate separation on the PTW 34013 ionization chamber was accounted for as a type B uncertainty for MC calculations. This geometric parameter was determined based on the tolerance in the electrode separation taken from the manufacturer sketches. The exact chamber dimensions are not provided in this paper as they are proprietary information. Additional MC simulations were run to obtain the absorbed dose rates to the ionization chamber when using chamber plate separations of maximum (thick) and minimum (thin) amplitude. Assuming equal probabilities of plate separations between the maximum and the minimum, a rectangular distribution on this uncertainty component was used according to: $\sigma_{\text{sep}} = 100\,(\dot{D}_{\text{thick}} - \dot{D}_{\text{thin}})/(2\sqrt{3}\,\dot{D}_{\text{nominal}})$, resulting in standard uncertainties of 2.0% and 0.9% at 10 and 40 mm, respectively. This leads to combined uncertainties (k = 1) for the ionization chamber calculations of 3.1% and 3.7% at the evaluation points. Uncertainties related to the microDiamond detector geometry, mass density and material composition were assumed to be negligible for the dose profile calculations (Rossi et al. 2019). In fact, the microDiamond detector active area and its diameter have been reported to be in good agreement with the corresponding nominal values, indicating a high stability in its construction, and negligible impact on the dose determination (Marinelli et al. 2016). The uncertainty budget for measurements and MC calculations is summarized in table 3.

Table 3. Uncertainty (k = 1) budget for dose rate measurements and MC calculations with the PTW 34013 ionization chamber and the synthetic diamond detectors. All uncertainties are expressed as percentages.

	$\dot{D}$(10 mm, 0°)		$\dot{D}$(40 mm, 0°)	
Uncertainty component	Type A (%)	Type B (%)	Type A (%)	Type B (%)
Measurement uncertainties				
Ionization chamber				
Measurement repeatability	0.02		0.09	
Source-detector distance		2.2		0.7
Combined standard uncertainty	**2.2**		**0.7**	
microDiamond detector (averaged)				
Measurement repeatability	0.2		0.3	
Source-detector distance		14.0		4.8
Combined standard uncertainty	**14.0**		**4.8**	
MC calculation uncertainties				
Ionization chamber				
Statistical uncertainty	2.4		3.6	
Electrode separation		2.0		0.9
Combined standard uncertainty	**3.1**		**3.7**	
microDiamond detector				
Statistical uncertainty	0.7		1.0	
Standard uncertainty	**0.7**		**1.0**	
Dose to water				
Statistical uncertainty	0.07		0.3	
Standard uncertainty	**0.07**		**0.3**	

3. Results and Discussion

3.1. MC model validation

3.1.1. Measurements with ionization chamber. The MC calculated depth dose curve for the INTRABEAM source in a water phantom is shown in figure 4(a), along with the measurements performed in a Zeiss water phantom using the PTW 34013 ionization chamber and an INTRABEAM source (denoted as *Source 1*), and a second set of measurements obtained by Watson et al. (2017) using a different INTRABEAM source (denoted as *Source 2*). All curves are normalized to unity at a depth of 10 mm from the source tip, just outside of the rapid dose fall-off region. Figure 4(b) presents the local relative differences of the MC simulation to the measurements with *Source 1* and *Source 2*. Due to the steep fall-off in dose close to the source, a sub-millimeter shift in the EPOM position was required for both sets of measurements and was calculated as 0.8 mm, on average.

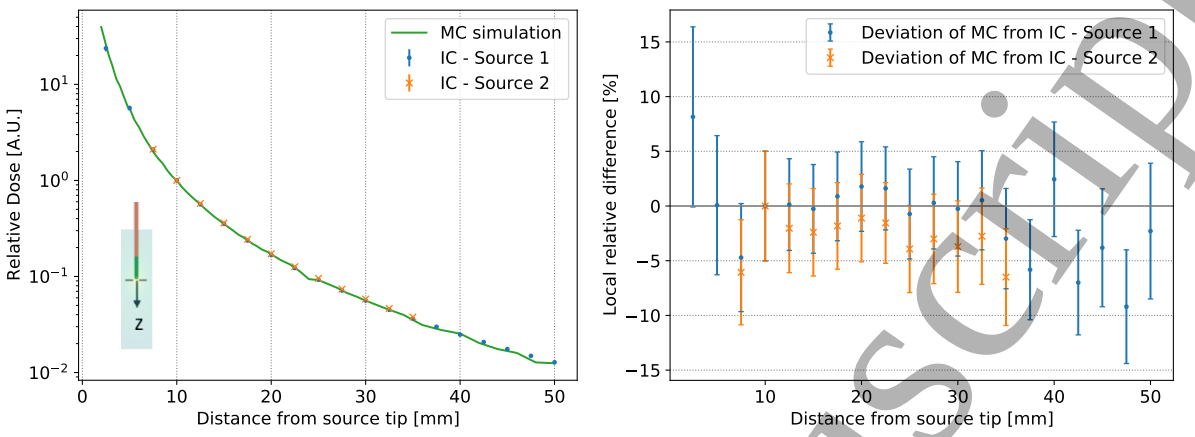

(a) (b)

Figure 4. (a) Comparison of the MC calculated depth doses to the ionization chamber in water, $(D_{\mathrm{RSV=air}})_{\mathrm{w}}$, for the INTRABEAM versus the measurements in the Zeiss water phantom using the PTW 34013 ionization chamber and an INTRABEAM source (*Source 1*) and the measurements with a second source (*Source 2*) by Watson et al. (2017). All curves are normalized at a depth of 10 mm from the source tip. The deviations from MC simulations to measurements with both sources are presented in (b) as local relative differences.

When looking at depths beyond 10 mm from the source in figure 4(b), MC calculations exhibit local relative differences from measurements with *Source 1* of up to 9%. At these depths, absolute differences varied from -0.2% to 0.3% of the value at the reference point, agreeing with the measurements within k = 2 standard uncertainties. Similarly, local relative differences between our MC calculations and the measurements with *Source 2* reached up to 6%, in the water depth range of 7.5 to 35 mm. Beyond 10 mm distances from the source, absolute differences varied within the range 0.1% to 1.2%, validating the MC model, within k = 2 measurement uncertainties. Measurements close to the source tip exhibit a relative difference of up to 8% at 2.5 mm depth from *Source 1* and 6% for *Source 2* at 7.5 mm. In this region, uncertainties due to positioning dominated over other factors, with higher impact in the dose estimation. These discrepancies can be attributed to several factors. Averaging volume effects occur in the rapid fall-off of the dose near the source along the finite RSV of the detector affecting its performance. Furthermore, the MC simulations are dependent on the geometry of the ionization chamber employed, which for the PTW 34013 model represents a significant source of uncertainty (Watson et al. 2017, Watson et al. 2018). The energy spectrum of the low-energy kV x rays varies significantly with depth in water, as the beam hardens, with demonstrated variations of HVLs of 0.1 to 2 mm Al over a distance of 20 mm (Watson et al. 2017). The spectral variations can alter the response of the detector during measurements. Nevertheless, the energy response of the detector is also accounted for in the simulations of dose to the RSV.

Different outputs are observed for measurements with *Source 1* and *Source 2*. The

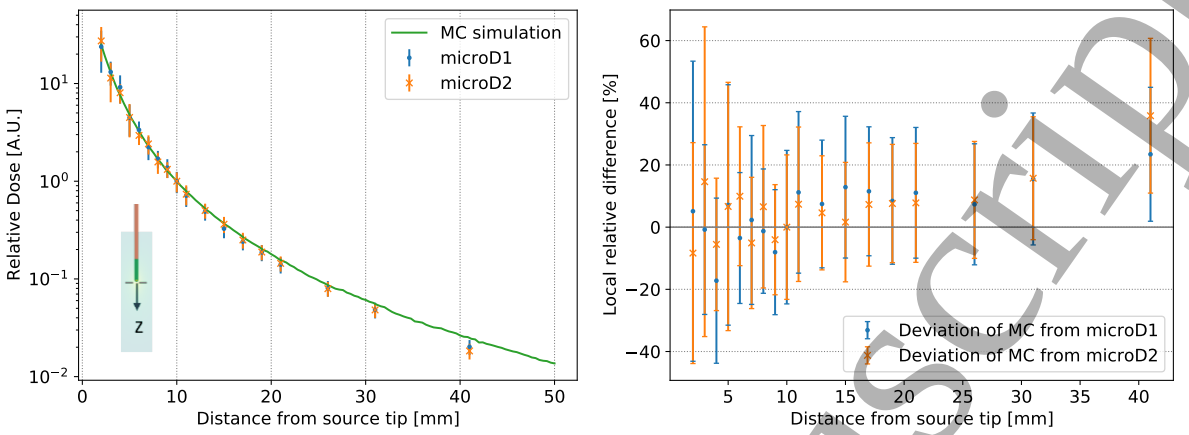

(a) (b)

Figure 5. (a) Comparison of the MC calculated depth doses to the diamond detector in water, $(D_{\mathrm{RSV=diam}})_{\mathrm{w}}$, for the INTRABEAM versus the measurements with the Wellhöfer 2D scanning system using two PTW TN60019 microDiamond detectors. All curves are normalized at a depth of 10 mm from the source tip. The deviations from MC simulations to measurements with both detectors are presented in (b) as local relative differences.

variations in the dose rate readings for different sources have also been reported in other studies (Armoogum et al. 2007, Moradi et al. 2017), and can result from differences in manufacturing of the source parts involved in the x-ray beam generation and the ideal geometry modeled in the MC codes. Some of the most relevant components contributing to the variation in output include the gold target thickness and shape, as well as the internal electron beam distribution determined by the electron gun and the magnetic deflector. These differences affect the beam effective energy and slightly change the spectrum at the source or applicator output, and are reflected in the depth dose curves as variations in the beam penetration power.

3.1.2. Measurements with microDiamond detectors. Results of the MC simulations of dose to the diamond RSV of the PTW TN60019 microDiamond detector were also compared with the measurements performed with the PTW TN60019 detectors (denoted as *microD1* and *microD2*) and the Wellhöfer water phantom and scanning system as shown in figure 5(a). Figure 5(b) presents the local relative differences of the MC simulation to the measurements with *microD1* and *microD2*. Due to the steep fall-off in dose close to the source, a sub-millimeter average correction of 0.3 mm in the EPOM positioning for both sets of measurements was required.

Agreement between measured data and the MC simulations is observed in the range of depths presented in figure 5(b) within uncertainties. However, positioning uncertainties with the Wellhöfer water phantom/microDiamond detector system were higher since the INTRABEAM source is manually adjusted in a vertical position right above and parallel to the detector location and displacement. A precision of 0.5 mm

was given to source positioning with the Wellhöfer water phantom setup, as compared with the 0.1 mm precision obtained with the Zeiss water phantom. Accounting for these uncertainties, agreement was observed with the microDiamond detector at closer distances from the source tip. The relative deviations of the calculations to the measurements at points located at less than 10 mm from the source tip, along the source axis, exhibit average values of 6% and 5% for the microDiamond detector and the ionization chamber, respectively. Larger discrepancies at more distal positions were attributed to decreased signal and the increased relative contribution of leakage current in the detection system. However, the differences fell within the estimated combined uncertainties at all depths. The trend in the deviation from MC to measurements was not observed during the ionization chamber measurements due to its larger RSV, with a relation of 1250:1 as compared to the nominal RSV of the microDiamond detector. The larger sensitive volume allowed the ionization chamber to collect a higher charge for measurements further away from the source, increasing the signal-to-noise ratio.

3.2. Radial dose function

The MC simulated radial dose function data for the bare probe of the INTRABEAM, using the *ring-shaped source* model, are presented in table 4 for distances to source tip ranging from 2 to 50 mm at a polar angle $\theta = 90°$. The functional behaviour of the INTRABEAM source can be deduced from the curve in figure 6 and it can be compared to the radial dose function reported for the updated version of the Xoft Axxent source (Hiatt et al. 2015) operated at 50 kV and some common brachytherapy radionuclides described in the AAPM TG-43U1 report, namely ^{192}Ir, ^{125}I and ^{103}Pd (Rivard et al. 2004). When compared to other sources, the dose rate from the INTRABEAM source decreases with a steeper gradient close to the source surface and then, after ∼20 mm depth, the fall-off slope becomes similar to that of the Xoft and the ^{125}I sources. The difference from the Xoft source is due to its materials and design, including the source target, walls, filters and biocompatible layers. Among these components, the main contributing factor is the target material of gold for INTRABEAM and tungsten for Xoft. Different studies have shown the spectra of the INTRABEAM with predominant fluorescence peaks observed at the L-lines of gold (in the range 9 to 14 keV) and K-lines of nickel (7.5 and 8.3 keV), and a mean photon energy of ∼19 keV at the source tip (Watson et al. 2017, Yanch & Harte 1996, Nwankwo et al. 2013, Moradi et al. 2017). For the Xoft source, fluorescence peaks at the K-lines of yttrium (15 and 17 keV) in the tungsten anode substrate are predominant, and a mean photon energy of ∼26.7 keV for the beam output is reported (Rivard et al. 2006). At energies higher than ∼17 keV, the spectra of the two sources are similar. The lower mean energy at the output of the INTRABEAM source, followed by a progressive beam hardening with depth in water, explains the rapid dose rate fall-off near the INTRABEAM, as compared with the Xoft source, and the similitude of the dose gradient at larger distances. The type A uncertainties, with coverage factor 1 (k = 1), from the

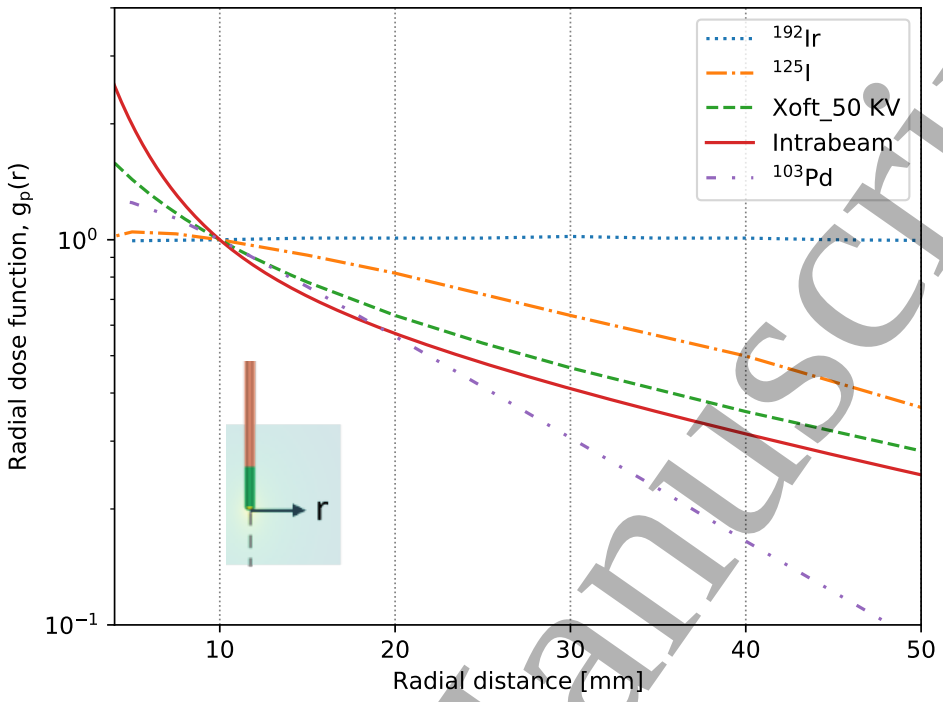

Figure 6. Radial dose function of the INTRABEAM source compared to the Xoft source operated at 50 kV (Hiatt et al. 2015) and common brachytherapy sources ^{192}Ir, ^{125}I and ^{103}Pd.

MC simulations varied from 0.01% to 0.02% at radial distances of 2 to 50 mm.

3.3. 2D anisotropy function

Figure 7 presents the results of the TG-43 2D anisotropy function calculations for the *ring-shaped source* model of the INTRABEAM. Due to the azimuthal symmetry, a map of the calculated 2D anisotropy can be fully represented in a semicircle, as shown in figure 7(a). Figure 7(b) displays the 2D anisotropy data as a function of polar angle (θ) for the *ring-shaped source* model, and compares it with the 2D anisotropy function calculated for the *spotted-shaped source* model. There are several aspects of the 2D anisotropy parameter that can be inferred from figure 7. For instance, the effect of the beryllium window in the distal 16 mm of the probe is highlighted by significantly larger anisotropy values, close to the source surface, as compared with the remarkably low values near the probe surface in more proximal positions, where the beryllium window is replaced by nickel walls that internally shield most of the incoming back-scattered radiation from the gold target. The effect is also observed in the curves of figure 7(b). For smaller radii ($r < 16$ mm), the function increases as moving towards larger theta values, approaching the beryllium window, whereas for curves of $r > 16$ mm a flip in the curves slope, from positive to negative, is noticeable at around $\theta = 155°$ when approaching the nickel walls. 2D anisotropy values are calculated only outside the

Table 4. MC calculated radial dose function data, $g_{\mathrm{p}}(r)$, and their associated type A uncertainty, using the TG-43 point-source model for the INTRABEAM source.

r (mm)	$g_{\mathrm{p}}(r)$	uncertainty (%)
2	4.782	0.013
4	2.510	0.012
6	1.645	0.011
8	1.232	0.010
10	1.000	0.009
12	0.854	0.009
14	0.753	0.010
16	0.678	0.010
18	0.619	0.010
20	0.571	0.010
22	0.530	0.011
24	0.495	0.011
26	0.464	0.012
28	0.436	0.012
30	0.411	0.012
32	0.388	0.013
34	0.367	0.013
36	0.348	0.014
38	0.330	0.014
40	0.313	0.015
42	0.298	0.015
44	0.283	0.016
46	0.270	0.016
48	0.257	0.017
50	0.245	0.018

source and that explains the reduced arc covered by shorter radii in the graph. Three main regions can be observed in the distribution of the 2D anisotropy function with two brighter yellow solid angle regions divided by a darker blue region in the range $\theta \approx [55^{\circ}, 130^{\circ}]$. The larger intensity regions towards the distal and proximal directions of the source are generated by the primary beam transmission at the gold target and the back-scattered component, respectively. This behaviour is depicted by the radii of incidence of the electron beam onto the hemispherical target after being internally deflected. It is worth recalling here that the reference line for the 2D anisotropy function ($\theta = 90^{\circ}$) was set on the plane traversing the source tip, and not on the plane traversing the effective photon source position. The effective source is located inside the gold target hemisphere, a few millimeters above the source tip. Specifically, it should be located between ∼0.8 mm, corresponding to the center of curvature of the hemispheric component of the probe tip (Yanch & Harte 1996) and ∼0.9 mm, enclosing the region of impact of the electron beam onto the gold target for the *ring-shaped source* and the *spotted-shaped source* models (Schneider 2017). The reference selection at the external surface of the probe tip causes the dark blue region in the proximity of the source end

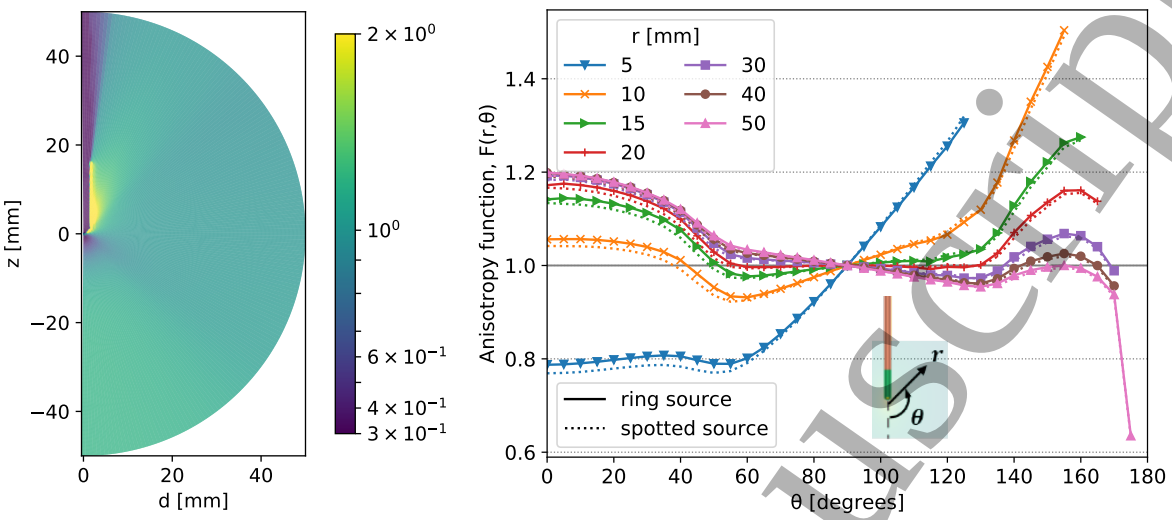

(a) (b)

Figure 7. (a) 2D anisotropy function map calculated for the INTRABEAM source using the *ring-shaped source* model. (b) 2D anisotropy function curves obtained for the *ring-shaped source* (solid) and the *spotted-shaped source* (dotted) models in the range $\theta = [0°, 180°]$ at several distances from the source tip.

towards the distal direction. The behaviour is only observed close to the source tip where the distance to the effective source position in the steep dose gradient dominates over the general dose distribution resulting from the internal electron beam deflection.

As observed in figure 7(b), the *ring-shaped source* and the *spotted-shaped source* models show a similar behaviour, with relative differences of up to 0.3% towards the central axis of the source probe, and all the described features of the 2D anisotropy parameter apply for both models. The difference in the 2D anisotropy function was not significant when compared to the calculation uncertainties, therefore, the *ring-shaped source* model was kept as reference for our study. The effect of the internal beam deflection in the dose distribution isotropy was also assessed by comparing the 2D anisotropy function of the *ring-shaped source* model with that of the homogeneous *circular-shaped source*. The results (not shown in figure 7) indicated an increase in isotropy of less than 1.0% around the INTRABEAM source when incorporating the electron beam oscillation not present in the *circular-shaped source*. Calculated data for the *ring-shaped source* model are presented in table 5 for polar angles 0° to 175° in steps of 5° and radial distances ranging from 2 to 50 mm.

The 2D anisotropy data from the study by Shamsabadi et al. (2020) for the bare source are in agreement with our data for $r = 10$ mm shown in figure 7(b), however, the polar angle interval covering up 130°, is smaller in their study compared to ours.

Figure 8 compares the 2D anisotropy function of the *ring-shaped source* model of the INTRABEAM source with the 2D anisotropy reported for the Xoft source (Hiatt et al. 2015). In general, the behavior of the function in the forward directed quadrant

Table 5. MC calculated 2D anisotropy function data, $F(r,\theta)$, for the bare probe of the INTRABEAM source with the *ring-shaped source* model. Points located inside the source, for which $F(r,\theta)$ is not determined, are indicated by 'NA'.

	Radial distance, r (mm)								
Polar angle, θ (°)	2	4	6	8	10	20	30	40	50
0	0.394	0.686	0.868	0.982	1.056	1.172	1.192	1.199	1.199
5	0.395	0.686	0.869	0.983	1.056	1.175	1.192	1.195	1.196
10	0.399	0.689	0.870	0.984	1.057	1.172	1.189	1.192	1.192
15	0.404	0.693	0.873	0.984	1.055	1.167	1.183	1.186	1.187
20	0.410	0.699	0.875	0.983	1.052	1.160	1.175	1.178	1.179
25	0.417	0.706	0.876	0.981	1.047	1.150	1.165	1.168	1.169
30	0.428	0.712	0.877	0.977	1.040	1.138	1.152	1.155	1.156
35	0.441	0.718	0.876	0.970	1.029	1.122	1.136	1.139	1.140
40	0.453	0.721	0.869	0.957	1.012	1.099	1.114	1.118	1.120
45	0.467	0.721	0.854	0.933	0.982	1.064	1.080	1.087	1.091
50	0.485	0.721	0.840	0.910	0.953	1.029	1.048	1.057	1.064
55	0.509	0.728	0.834	0.895	0.934	1.004	1.024	1.035	1.043
60	0.541	0.746	0.842	0.897	0.932	0.997	1.016	1.026	1.034
65	0.584	0.775	0.860	0.909	0.939	0.996	1.013	1.022	1.028
70	0.640	0.811	0.884	0.925	0.950	0.997	1.010	1.018	1.022
75	0.707	0.852	0.911	0.942	0.962	0.999	1.008	1.014	1.017
80	0.786	0.898	0.939	0.961	0.975	1.000	1.006	1.009	1.012
85	0.883	0.947	0.969	0.981	0.988	1.000	1.003	1.005	1.006
90	1.000	1.000	1.000	1.000	1.000	1.000	1.000	1.000	1.000
95	NA	NA	1.031	1.019	1.012	1.000	0.997	0.995	0.994
100	NA	NA	1.063	1.037	1.023	1.000	0.993	0.990	0.988
105	NA	NA	1.094	1.057	1.035	0.998	0.989	0.985	0.982
110	NA	NA	1.127	1.076	1.046	0.996	0.984	0.979	0.976
115	NA	NA	1.159	1.093	1.054	0.992	0.980	0.974	0.969
120	NA	NA	1.187	1.107	1.066	0.997	0.979	0.970	0.965
125	NA	NA	1.235	1.148	1.093	0.996	0.973	0.963	0.957
130	NA	NA	1.318	1.191	1.119	1.001	0.973	0.961	0.954
135	NA	NA	1.440	1.270	1.178	1.026	0.988	0.971	0.962
140	NA	NA	NA	1.389	1.268	1.070	1.018	0.994	0.979
145	NA	NA	NA	1.503	1.351	1.107	1.041	1.009	0.990
150	NA	NA	NA	NA	1.425	1.135	1.056	1.019	0.997
155	NA	NA	NA	NA	1.504	1.160	1.068	1.026	1.000
160	NA	NA	NA	NA	NA	1.161	1.064	1.020	0.994
165	NA	NA	NA	NA	NA	1.138	1.040	1.000	0.976
170	NA	NA	NA	NA	NA	NA	0.989	0.956	0.938
175	NA	NA	NA	NA	NA	NA	NA	NA	0.635

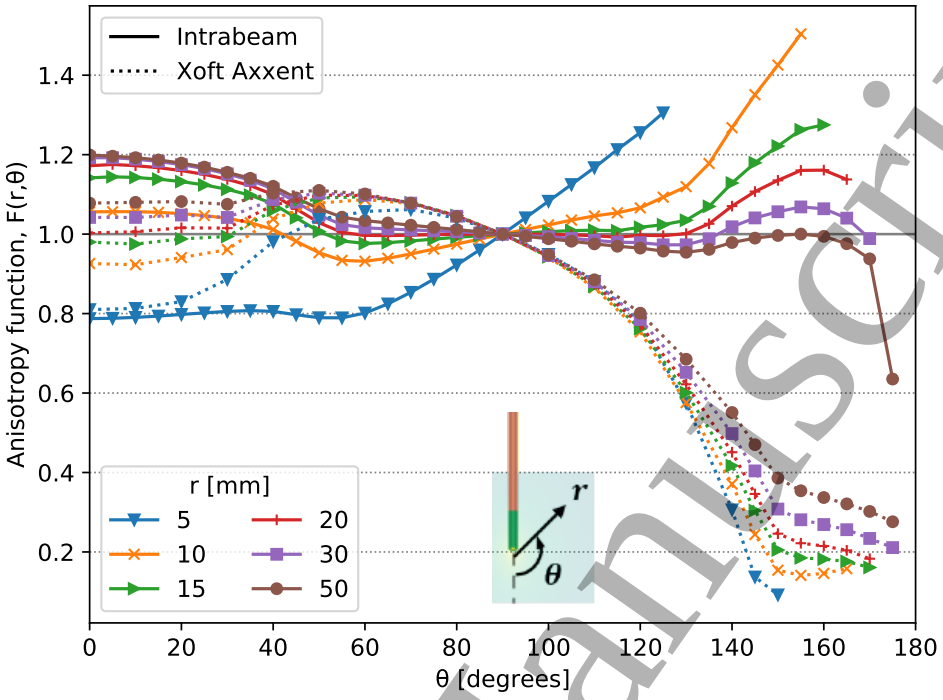

Figure 8. Radial dose function of the INTRABEAM source compared to the Xoft source operated at 50 kV (Hiatt et al. 2015) and common brachytherapy sources ^{192}Ir, ^{125}I and ^{103}Pd.

(θ = [0°,90°]) is similar for both eBT sources with less than 16% absolute difference, except in the proximal region of r = 5 mm where the difference reached up to 26%. The marked deviation at 5 mm might be related to the selection of the source origin which for the Xoft model was placed at the effective source location, at the center of the x-ray anode cone, instead of the external surface of the needle, as used for the INTRABEAM model. For both eBT sources, the larger 2D anisotropy values are observed in the proximal quadrant of the source (θ = [90°, 180°]). In both cases, the 2D anisotropy deviation from unity increased as evaluated closer to the source origin in the radial direction, and as moving towards the source axis in the angular direction, with maximal absolute differences between sources of 48% at $P(r = 5$ mm, $\theta = 120°)$, 136% at $P(r = 10$ mm, $\theta = 155°)$ and 109% at $P(r = 15$ mm, $\theta = 160°)$. This behaviour could be attributed to the large Beryllium x-ray window used in the distal part of the Zeiss needle, which is not present in the Xoft Axxent model.

It should be noted, however, that the 2D anisotropy function presented in this study is evaluated for the bare probe and is not accounting for attenuation and scattering of the beam when using clinical applicators. In this context, Shamsabadi et al. (2020) have recently developed a Geant4 MC model of the INTRABEAM system and evaluated the spectral and dosimetric characteristics of the beam with and without the use of spherical applicators. Their MC model was validated by comparing depth dose calculations in water along the source axis with the manufacturer's calibration report and verified

polar anisotropy at 1 cm from probe and applicator surfaces. Their results show that the presence of the applicators can increase the anisotropy observed around the bare probe.

In addition to the relative functions presented in this report, a complete characterization of the INTRABEAM source, according to the TG-43 formalism, requires the determination of the dose-rate constant in (1). Despite having the measurements of dose rates at the reference point for the source, Λ could not be determined for the INTRABEAM since the air-kerma strength has not been provided for the system. In fact, previous work with the Xoft source has shown that the determination of S_{K} for eBT sources is prone to significant uncertainties due to large scatter and attenuation corrections and variations in source-to-source manufacturing (DeWerd et al. 2015). Therefore, the National Institute of Standards and Technology (NIST) established a new standard for the calibration of the Xoft Axxent source based on a modification of the TG-43 formalism (Seltzer et al. 2014). In this variation, S_{K} is replaced by the air-kerma rate measured in air at 50 cm from the source, $\dot{K}_{50\mathrm{cm}}$, and Λ is replaced by χ, the dose-rate conversion coefficient at the reference point ($r_0 = 1$ cm, $\theta_0 = 90°$). In parallel to the NIST research, the National Metrology Institute of Germany (PTB) is developing a primary standard for eBT sources in terms of absorbed dose to water (Schneider et al. 2016). A recent publication by Abudra'a et al. (2020) reports the results of the PTB standard applied to the INTRABEAM system with a 4 cm diameter spherical applicator. At the time of this report, no accepted air-kerma-based primary standard is available for INTRABEAM sources. For this reason, our work does not include determination of the dose-rate constant Λ.

The original *circular-shaped source* model of the INTRABEAM system, employed in previous works by Watson *et al* (2017, 2018, 2018), was modified in this study to evaluate the impact of the internal source electron deflections and its Gaussian distribution in energy to achieve a more accurate estimate of 3D dose distributions. In the previous reports, measurements and calculations were only performed along the source probe axis, with both ionization chamber and radiochromic film. In the present paper we set out to also map the dose distribution in the coronal plane of the source so as to arrive at the full TG-43 2D anisotropy function. The new data allowed to make dosimetric comparisons with other brachytherapy sources, especially with the TG-43 parameters of the Xoft source with the aim of contributing to the standardization of eBT dosimetry. In addition, the use of the microDiamond detectors, which was not covered in previous studies for the INTRABEAM, was investigated as an alternative detector able to reduce volume averaging uncertainties observed in other detectors in the steep dose fall-off in the proximity of the probe.

This study is limited to the characterization of the source in terms of its dose distribution in water, using homogeneous phantoms. However, in the low-energy range of x-rays from eBT sources, water cannot be assumed to be tissue equivalent due in part to the predominance of the photoelectric effect and its dependence on the atomic number of the media. Therefore, the extent of usability of the parameters derived herein need

to be carefully assessed in an application-based approach before their implementation in TPSs. Previous works have studied the impact of tissue inhomogeneities on dose calculation in the context of low-energy x-rays eBT sources. Bouzid et al. (2015) developed an in-house MC-based dosimetry platform using the Geant4 Application for Emission Tomography (GATE) to perform CT-based patient-specific dose calculations with the INTRABEAM system. Their MC model was subsequently used by Chiavassa et al. (2015), after some modifications in terms of physical processes, energy cuts and probe positions, to evaluate the effects of inhomogeneous media in pelvic region. The results of their study showed an increment of ∼6% in the obtained dose to rectum, bladder and target, when assuming water instead of the real tissue composition. This relatively small variation in results is explained by the small difference in the effective atomic number, which is 7.56 for soft tissue, 7.85 for muscle and 7.73 for water. However, they found large increments in mean dose to symphysis and ischiopubic bones of 180% and 227%, respectively, relative to the calculations in water. A reduction in dose of 10–20% close to an air cavity was also reported, explained as a lack of backscatter in air relative to water. The variability in tissue type also plays an important role in the relative biological effectiveness (RBE) of the beam quality used. The RBE of eBT low-energy photons has proven to be larger than that of greater photon energies of other radiotherapy modalities. For instance, White et al. (2016) investigated the RBE of eBT sources in different breast tissues, accounting for spectral and beam quality variations due to source design, use of applicators and depth in tissue. They found similar RBE values for the Xoft and INTRABEAM sources, with 4 cm diameter applicators, ranging between 1.4 to 1.6 with reference to cobalt-60. Variations in RBE values were correlated to tissue type as demonstrated in rib, gland, adipose, skin and lung with RBE values of ∼1.4, ∼1.55, ∼1.59, ∼1.52 and ∼1.50, respectively.

Work is in progress to determine the relative TG-43 dosimetry parameters for the system containing spherical applicators. These data are required by commercial TPSs since all clinical cases are conducted with the use of applicators. We are especially interested in the calculation of 3D dose distributions in brain tissues, in the context of the INTRAGO protocol, as this information is necessary to accurately estimate the total radiation doses received by the tumour bed and the organs at risk in the adjuvant IORT + EBRT plans. Evaluation of the effect of tissue inhomogeneities will be addressed by comparing the results from the TG-43 approach with CT-based MC calculated dose distributions. RBE ought to be considered in the evaluation of treatment plans from different techniques.

4. Conclusion

In this study, the radial dose function, $g_{\mathrm{p}}(r)$, and the 2D anisotropy function, $F(r,\theta)$, recommended by the AAPM TG-43 as dosimetric parameters for brachytherapy sources, were calculated for the INTRABEAM miniature x-ray source using MC simulations. The MC model of the source was validated with depth dose measurements in water

using a PTW 34013 ionization chamber and two microDiamond PTW TN60019 detectors. Measurements in water with the ionization chamber showed agreement with the calculations at distances from the source beyond 10 mm. Detector geometry uncertainties were satisfactorily reduced with the use of the microDiamond detector, which has a smaller RSV that better accounts for volume averaging effects in steep dose gradient regions. However, positioning uncertainties with the alternative system are still high with the available setup. The work presented here sets the path to establish a metrology system for the INTRABEAM and validates the methodology for obtaining the data necessary for the characterization of the source as required by a TPS used in clinical dose calculations. Consequently, dosimetric comparison with other commonly available brachytherapy sources and treatment techniques is possible. Future work will utilize these data to enable the calculation of applicator-specific TG-43 parameters and further develop the INTRABEAM for clinical IORT. In addition, the suitability of the calculated TG-43 parameters for use in TPSs will be assessed by comparing the obtained dose distributions with the results in patient-specific MC simulations that account for tissue heterogeneities.

Acknowledgments

The authors wish to thank Dr. Tanner Connell who helped setting up the dosimetry system for INTRABEAM measurements, and Mr. Joe Larkin who built an accessory for measurements with the INTRABEAM arm without inclusion of applicators. D.S.A.A. acknowledges partial support by the CREATE Medical Physics Research Training Network grant of the Natural Sciences and Engineering Research Council (grant number: 432290) and the financial support from the Fonds de recherche du Québec – Santé (FRQS, grant number: 292924).

References

Abudra'A, A. (2017). *Development of new dosimetric standards for low energy X-rays (≤ 50 keV) used in contact radiotherapy*, PhD thesis, Université Paris-Saclay.

Abudra'a, A., Chauvenet, B., Gouriou, J., Plagnard, J., Itti, R. & Aubineau-Lanièce, I. (2020). Dosimetry formalism and calibration procedure for electronic brachytherapy sources in terms of absorbed dose to water, *Physics in Medicine & Biology* **65**(14): 145006.

Armoogum, K. S., Parry, J. M., Souliman, S. K., Sutton, D. G. & Mackay, C. D. (2007). Functional intercomparison of intraoperative radiotherapy equipment–Photon Radiosurgery System, *Radiation Oncology* **2**(1): 11.

Berger, M. J., Hubbell, J. H., Seltzer, S. M., Chang, J., Coursey, J. S., Sukumar, R., Zucker, D. S. & Olsen (2010). XCOM: Photon Cross Sections Database (version 1.5). [Online] Available: http://physics.nist.gov/xcom (accessed September 2020), *National Institute of Standards and Technology, Gaithersburg, MD* .
URL: *http://physics.nist.gov/xcom*

Biggs, D. S. & Thomson, E. S. (1996). Radiation properties of a miniature X-ray device for radiosurgery, *The British Journal of Radiology* **69**(822): 544–547.

BIPM, IEC, IFCC, ISO, IUPAC, IUPAP and OIML (1995). Guide to the Expression of Uncertainty in Measurement, *Geneva, Switzerland: International Organisation for Standardisation* .

Bote, D. & Salvat, F. (2008). Calculations of inner-shell ionization by electron impact with the distorted-wave and plane-wave Born approximations, *Physical Review A* **77**(4): 042701.

Bouzid, D., Bert, J., Dupre, P.-F., Benhalouche, S., Pradier, O., Boussion, N. & Visvikis, D. (2015). Monte-Carlo dosimetry for intraoperative radiotherapy using a low energy x-ray source, *Acta Oncologica* **54**(10): 1788–1795.

Carl Zeiss Meditec AG (2011). *INTRABEAM dosimetry, Brochure EN_30_010_155II.*

Carl Zeiss Meditec AG (2015). *INTRABEAM Water Phantom – Instructions for use, G-30-1767-en Version 5.0.*

Chamberland, M. J. P., Taylor, R. E. P., Rogers, D. W. O. & Thomson, R. M. (2016). egs_brachy: a versatile and fast Monte Carlo code for brachytherapy, *Physics in Medicine & Biology* **61**(23): 8214–8231.

Chiavassa, S., Buge, F., Hervé, C., Delpon, G., Rigaud, J., Lisbona, A. & Supiot, S. (2015). Monte Carlo evaluation of the effect of inhomogeneities on dose calculation for low energy photons intra-operative radiation therapy in pelvic area, *Physica Medica* **31**(8): 956–962.

Clausen, S., Schneider, F., Jahnke, L., Fleckenstein, J., Hesser, J., Glatting, G. & Wenz, F. (2012). A Monte Carlo based source model for dose calculation of endovaginal TARGIT brachytherapy with INTRABEAM and a cylindrical applicator, *Zeitschrift für Medizinische Physik* **22**(3): 197–204.

DeWerd, L. A., Culberson, W. S., Micka, J. A. & Simiele, S. J. (2015). A modified dose calculation formalism for electronic brachytherapy sources, *Brachytherapy* **14**(3): 405–408.

DeWerd, L. A., Ibbott, G. S., Meigooni, A. S., Mitch, M. G., Rivard, M. J., Stump, K. E., Thomadsen, B. R. & Venselaar, J. L. (2011). A dosimetric uncertainty analysis for photon-emitting brachytherapy sources: Report of AAPM Task Group No. 138 and GEC-ESTRO, *Medical physics* **38**(2): 782–801.

Dinsmore, M., Harte, K. J., Sliski, A. P., Smith, D. O., Nomikos, P. M., Dalterio, M. J., Boom, A. J., Leonard, W. F., Oettinger, P. E. & Yanch, J. C. (1996). A new miniature x-ray source for interstitial radiosurgery: Device description, *Medical Physics* **23**(1): 45–52.

Douglas, R. M., Beatty, J., Gall, K., Valenzuela, R. F., Biggs, P., Okunieff, P. & Pardo, F. S. (1996). Dosimetric results from a feasibility study of a novel radiosurgical source for irradiation of intracranial metastases, *International journal of radiation oncology, biology, physics* **36**(2): 443–450.

Eaton, D. (2012). Quality assurance and independent dosimetry for an intraoperative x-ray device, *Medical physics* **39**(11): 6908–6920.

Giordano, F. A., Brehmer, S., Abo-Madyan, Y., Welzel, G., Sperk, E., Keller, A., Schneider, F., Clausen, S., Herskind, C., Schmiedek, P. & Wenz, F. (2014). INTRAGO: intraoperative radiotherapy in glioblastoma multiforme – a Phase I/II dose escalation study, *BMC Cancer* **14**(1): 992.
URL: *https://doi.org/10.1186/1471-2407-14-992*

Gunderson, L. L., Willett, C. G., Calvo, F. A. & Harrison, L. B. (2011). *Intraoperative irradiation: techniques and results*, 2 edn, New York, NY, USA: Springer Science & Business Media.

Hiatt, J. R., Davis, S. D. & Rivard, M. J. (2015). A revised dosimetric characterization of the model S700 electronic brachytherapy source containing an anode-centering plastic insert and other components not included in the 2006 model, *Medical Physics* **42**(6Part1): 2764–2776.

Kaveckyte, V., Persson, L., Malusek, A., Benmakhlouf, H., Alm Carlsson, G. & Carlsson Tedgren, Å. (2020). Investigation of a synthetic diamond detector response in kilovoltage photon beams, *Medical Physics* **47**(3): 1268–1279.

Kawrakow, I., Mainegra-Hing, E., Tessier, F. & Walters, B. R. B. (2009). The EGSnrc C++ class library, NRC Report PIRS-898 (rev A), *Technical report*, National Research Council Canada, Ottawa, Canada.

Kawrakow, I. & Rogers, D. W. O. (2019). The EGSnrc code system: Monte Carlo simulation of electron and photon transport, *Technical Report PIRS-701*, National Research Council Canada, Ottawa, Canada.
URL: *http://nrc-cnrc.github.io/EGSnrc/doc/pirs701-egsnrc.pdf*

Marinelli, M., Prestopino, G., Verona, C. & Verona-Rinati, G. (2016). Experimental determination of the PTW 60019 microDiamond dosimeter active area and volume, *Medical physics* **43**(9): 5205–5212.

Moradi, F., Ung, N. M., Khandaker, M. U., Mahdiraji, G. A., Saad, M., Abdul Malik, R., Bustam, A. Z., Zaili, Z. & Bradley, D. A. (2017). Monte Carlo skin dose simulation in intraoperative radiotherapy of breast cancer using spherical applicators, *Physics in Medicine & Biology* **62**(16): 6550–6566.

Nath, R., Anderson, L. L., Luxton, G., Weaver, K. A., Williamson, J. F. & Meigooni, A. S. (1995). Dosimetry of interstitial brachytherapy sources: Recommendations of the AAPM Radiation Therapy Committee Task Group No. 43, *Medical Physics* **22**(2): 209–234.

Nwankwo, O., Clausen, S., Schneider, F. & Wenz, F. (2013). A virtual source model of a kilo-voltage radiotherapy device, *Physics in Medicine & Biology* **58**(7): 2363–2375.

Rivard, M. J., Coursey, B. M., DeWerd, L. A., Hanson, W. F., Saiful Huq, M., Ibbott, G. S., Mitch, M. G., Nath, R. & Williamson, J. F. (2004). Update of AAPM Task Group No. 43 Report: A revised AAPM protocol for brachytherapy dose calculations, *Medical Physics* **31**(3): 633–674.

Rivard, M. J., Davis, S. D., DeWerd, L. A., Rusch, T. W. & Axelrod, S. (2006). Calculated and measured brachytherapy dosimetry parameters in water for the Xoft Axxent X-Ray Source: An electronic brachytherapy sourcea), *Medical Physics* **33**(11): 4020–4032.

Rossi, G., Gainey, M., Thomann, B., Kollefrath, M., Würfel, J., Allgaier, B. & Baltas, D. (2019). Monte Carlo and experimental high dose rate 192Ir brachytherapy dosimetry with microDiamond detectors, *Zeitschrift für Medizinische Physik* **29**(3): 272–281.

Schneider, T. (2017). Towards reference dosimetry of electronic brachytherapy sources. *Metrology for Brachytherapy: State-of-the-art and beyond*, International Workshop (Braunschweig).

Schneider, T., Radeck, D. & Šolc, J. (2016). Development of a new primary standard for the realization of the absorbed dose to water for electronic brachytherapy x-ray sources, *Brachytherapy* **15**: S27–S28.

Sechopoulos, I., Rogers, D. W., Bazalova-Carter, M., Bolch, W. E., Heath, E. C., McNitt-Gray, M. F., Sempau, J. & Williamson, J. F. (2018). RECORDS: improved reporting of montE CarlO RaDiation transport studies: report of the AAPM Research Committee Task Group 268, *Medical physics* **45**(1): e1–e5.

Seltzer, S. M., O'Brien, M. & Mitch, M. G. (2014). New national air-kerma standard for low-energy electronic brachytherapy sources, *Journal of research of the National Institute of Standards and Technology* **119**: 554–574.

Sethi, A., Emami, B., Small Jr, W. & Thomas, T. O. (2018). Intraoperative radiotherapy with INTRABEAM: technical and dosimetric considerations, *Frontiers in oncology* **8**: 74.

Shamsabadi, R., Baghani, H. R., Azadegan, B. & Mowlavi, A. A. (2020). Monte Carlo based analysis and evaluation of energy spectrum for low-kV IORT spherical applicators, *Zeitschrift für Medizinische Physik* **30**(1): 60–69.

Sievers, P., Schneider, T., Michel, T. & Anton, G. (2011). X-ray spectroscopy with photon counting imaging detectors such as Timepix, *2011 IEEE Nuclear Science Symposium Conference Record*, IEEE, pp. 1826–1828.

Valdivieso-Casique, M. F., Rodríguez, R., Rodríguez-Bescós, S., Lardíes, D., Guerra, P., Ledesma, M. J., Santos, A., Ibáñez, P., Vidal, M., Udías, J. M., Otaduy, M. A., Calama, J. A., López-Tarjuelo, J., Santos-Miranda, J. A., Desco, M., García-Vázquez, V., Marinetto, E., Pascau, J., Calvo, F. & Illana, C. (2015). Radiance—a planning software for intra-operative radiation therapy, *Translational Cancer Research* **4**(2): 196–209.

Vidal, M., Ibáñez, P., González, J. C., Guerra, P. & Udías, J. (2014). Hybrid Monte Carlo dose

algorithm for low energy X-rays intra-operative radiation therapy, *Radiotherapy and Oncology* **111**: S106–S107.

Watson, P. (2019). *Dosimetry of a Miniature X-ray Source Used in Intraoperative Radiation Therapy*, PhD thesis, McGill University Libraries.

Watson, P. G. F., Bekerat, H., Papaconstadopoulos, P., Davis, S. & Seuntjens, J. (2018). An investigation into the INTRABEAM miniature x-ray source dosimetry using ionization chamber and radiochromic film measurements, *Medical Physics* **45**(9): 4274–4286.

Watson, P. G. F., Popovic, M. & Seuntjens, J. (2017). Determination of absorbed dose to water from a miniature kilovoltage x-ray source using a parallel-plate ionization chamber, *Physics in Medicine & Biology* **63**(1): 015016.

Watson, P. G. & Seuntjens, J. (2016). Effect of explicit M and N-shell atomic transitions on a low-energy x-ray source, *Medical physics* **43**(4): 1760–1763.

White, S. A., Reniers, B., De Jong, E. E., Rusch, T. & Verhaegen, F. (2016). A comparison of the relative biological effectiveness of low energy electronic brachytherapy sources in breast tissue: a Monte Carlo study, *Physics in Medicine & Biology* **61**(1): 383.

Wulff, J., Zink, K. & Kawrakow, I. (2008). Efficiency improvements for ion chamber calculations in high energy photon beams, *Medical Physics* **35**(4): 1328–1336.

Yanch, J. C. & Harte, K. J. (1996). Monte Carlo simulation of a miniature, radiosurgery x-ray tube using the ITS 3.0 coupled electron-photon transport code, *Medical Physics* **23**(9): 1551–1558.